

A chemical bond-based machine learning model for dipole moment: Application to dielectric properties of liquid methanol and ethanol

Tomohito Amano,¹ Tamio Yamazaki,² and Shinji Tsuneyuki¹

¹*Department of Physics, The University of Tokyo, Hongo, Bunkyo-ku, Tokyo 113-0033, Japan*

²*JSR-UTokyo Collaboration Hub, CURIE, JSR Corporation, 1-9-2, Higashi-Shinbashi, Minato-ku, Tokyo 105-8640, Japan*

(Dated: July 12, 2024)

We introduce a versatile machine-learning scheme for predicting dipole moments of molecular liquids to study dielectric properties. We attribute the center of mass of Wannier functions, called Wannier centers, to each chemical bond and create neural network models that predict the Wannier centers for each chemical bond. Application to liquid methanol and ethanol shows that our neural network models successfully predict the dipole moment of various liquid configurations in close agreement with DFT calculations. We show that the dipole moment and dielectric constant in the liquids are greatly enhanced by the polarization of Wannier centers due to local intermolecular interactions. The calculated dielectric spectra agree well with experiments quantitatively over terahertz (THz) to infrared regions. Furthermore, we investigate the physical origin of THz absorption spectra of methanol, confirming the importance of translational and librational motions. Our method is applicable to other molecular liquids and can be widely used to study their dielectric properties.

I. INTRODUCTION

Dielectric properties represent the interaction between electric fields and materials. Optical spectroscopy is a widely used technique to study the structure and dynamics of bulk systems. Simulation of the dielectric properties of materials with strong intermolecular interactions, such as liquid alcohols, is essential for interpreting experimental spectra.

Analyzing how polarization occurs is the key to comprehending the dielectric properties of liquid alcohol. In the liquid phase, the electric field generated by the surrounding molecules distorts the electronic cloud, resulting in different polarization features from the gas phase. Hydrogen bonding is an important intermolecular interaction appearing in polar molecules. Alcohol molecules, consisting of both polar hydroxyl and non-polar alkyl groups, can accept two hydrogen bonds (H-bonds) and only donate one H-bond, unlike water molecules that can donate two H-bonds. This difference leads to the distinct hydrogen bonding in alcohols compared to water [1, 2], thus resulting in the unique dielectric properties of alcohols. The dielectric constant at 300 K reaches 78 for water, while it is only 33 for methanol [3]. In the region below 1000 cm^{-1} (THz region), which is dominated by the intermolecular modes, the dielectric absorption of water has a translational (H-bond stretching) peak around 200 cm^{-1} and a libration peak around 600 cm^{-1} [4]. Although methanol also has a libration peak around 700 cm^{-1} [5–8], its lower frequency spectrum is more complex than that of water. THz spectroscopy experiments [9–12] pointed out three major peaks at around 60, 120, and 270 cm^{-1} using the Lorentzian fitting, with the 120 cm^{-1} one being the largest. The 270 cm^{-1} peak is broad and is thought to originate from intermolecular motions [5]. H-bond fluctuations, observed in the similar frequency region in experiments [1, 13], are likely asso-

ciated with these modes. However, the origins of these peaks are not yet fully understood.

After Rahman [14] introduced the classical molecular dynamics (CMD) method in 1964, the dielectric function of a system can be calculated from the dipole autocorrelation function along CMD trajectories based on the linear response theory [15]. The dipole moment \mathbf{M} is calculated by assigning an empirical charge q_i to the atom \mathbf{r}_i as $\mathbf{M} = \sum_i q_i \mathbf{r}_i$. Despite the rather simple description of dipole moments, CMD has been successfully used to study dielectric properties. As for THz absorption of methanol, early studies [16–19] identified a significant peak around 700 cm^{-1} to the hydroxyl H rotational (librational) motion around the CO axis, nearly parallel to the axis of the least inertia. Skaf et al. [17, 18] quantitatively reproduced lower the 60 and 120 cm^{-1} absorption peaks, which were imputed to the libration around the second-largest and largest principal inertia axes, respectively [16, 19–22]. Additionally, considering the induced dipole moments improved the agreement with experiments [23]. Torii [24] demonstrated that the induced dipole moments significantly contributed to the low-frequency peaks, while the rotation of the permanent molecular dipoles accounted for the 700 cm^{-1} peak of methanol by incorporating the induced dipole moments through H-bond stretching.

Although empirical force field approaches have been widely employed in studies on liquid alcohols, qualitative agreement with experimental values of the dielectric constant [25, 26] and the dielectric function [17, 19, 24] remains challenging due to the lack of explicit many-body induced polarization effects.

Car and Parrinello developed the *ab initio* molecular dynamics (AIMD) method [27], in which the atomic forces are calculated directly from first principle electronic structure calculations without empirical parameters. Furthermore, the modern theory of polarization [28, 29] can express the dipole moment in a quan-

tum mechanics manner through the maximally-localized Wannier function (MLWF) method [30, 31], where the electronic contribution to the dipole moment is evaluated from the $-2e$ point charges at the centers of MLWFs, known as Wannier centers (WCs). Accurate estimation of dynamics and polarization has led to numerous studies on liquid alcohols focusing on structure [32–36], hydrogen bonding [37–39], dipole moments [2, 40], and dielectric properties [41–44]. These studies have been elucidating the influence of the local atomic environment on dielectric properties. The average molecular dipole moment in the liquid methanol calculated from AIMD ranged from 2.5 D to 2.9 D [34, 37, 41, 43], which was larger than those obtained from force-field calculations [45]. Pagliai et al. [37] showed that the number of H-bonds strongly influenced the molecular dipole moments. Wang et al. [44] successfully reproduced the experimental dielectric function of liquid methanol using Born-Oppenheimer molecular dynamics (BOMD), showing significant improvement compared to the Car-Parrinello molecular dynamics (CPMD) calculation, which suffered from a large redshift in the spectrum around 3000 cm^{-1} [41]. For THz dielectric spectra, studies on liquid water unveiled the importance of the polarization of WCs due to intermolecular interactions [4, 46, 47]. In contrast, the THz spectra calculation of liquid methanol has not been done so often [42].

Recently, machine learning (ML) methods have been employed to express *ab initio* potential energy surfaces as a function of nuclear coordinates [48–52]. These methods preserve the accuracy of AIMD while improving its efficiency. To calculate dielectric properties using this technique, however, we also need ML models to predict the dipole moment from atomic positions. To this end, Gastegger et al. [53] constructed a model that learns the environment-dependent atomic partial charges, which vary depending on the positions of neighborhood atoms, and thus effectively describes the polarization effect of electrons in gas phase molecules. This scheme has been successfully applied to clusters [54, 55] and liquid structures [56, 57] and has been utilized to incorporate long-range Coulomb interactions into ML molecular dynamics [58, 59]. This atomic charge model has been adapted with ML models to learn dipole or multipole moments using ordinary ML methods [60–62] or graph-neural networks [63–65].

An alternative approach is to directly handling WCs. Several authors constructed ML models to predict the average position of the WCs in a water molecule, called the Wannier centroid, and successfully reproduced dielectric properties [62, 66–69]. To accurately predict vector quantities such as WCs, the models must be rotationally equivariant when the reference coordinate system is rotated. Zhang et al. [67, 68] addressed this requirement by using two networks, referred to as embedding and fitting networks. While a water molecule only has four WCs, larger molecules contain a larger number of WCs, making predicting the centroids more difficult. To overcome this challenge, we aim to extend this method to construct

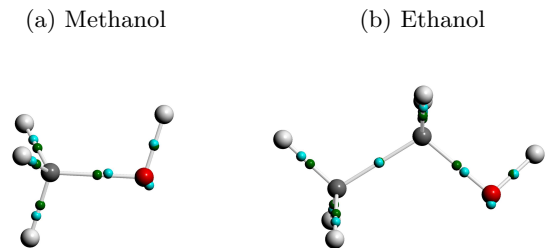


FIG. 1: Illustration of methanol (left) and ethanol (right) molecules. Oxygen, carbon, and hydrogen are represented by red, gray, and white spheres, respectively. Bond centers (BCs) and WCs are represented by small green and blue spheres. Only one blue circle is visible for the O lone-pair (lp), as it is the center of gravity of the two Wannier center (WC).

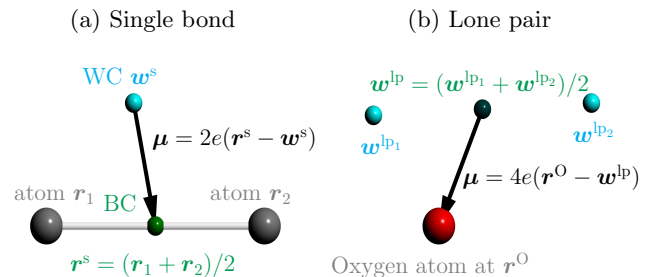


FIG. 2: Schematic image of dipole moments for a single bond and lone pair. \mathbf{r} represents the position of BCs.

ML models for each WC rather than the Wannier centroid.

In this work, we propose a versatile ML model to predict WCs applicable to molecular liquids. We assign WCs to chemical bonds between atoms and use deep neural networks to predict the position of the WC for each bond. WCs are collected by DFT calculations and used as training data for ML. To ensure the equivariance of the models, we followed the method by Zhang et al. [67]. We applied our method to calculate the dielectric properties of liquid methanol and ethanol. The ML models accurately predict the molecular dipole moments and reproduce the experimental dielectric properties well in the THz region, combined with AIMD trajectories.

II. THEORY

A. Dipole Moments

Evaluating dielectric properties requires the total dipole moments of the system during molecular dynamics (MD) simulations. In the MLWF method [30, 31], the total dipole moment of a bulk periodic system consists of the ion-core and the valence-electronic parts. The

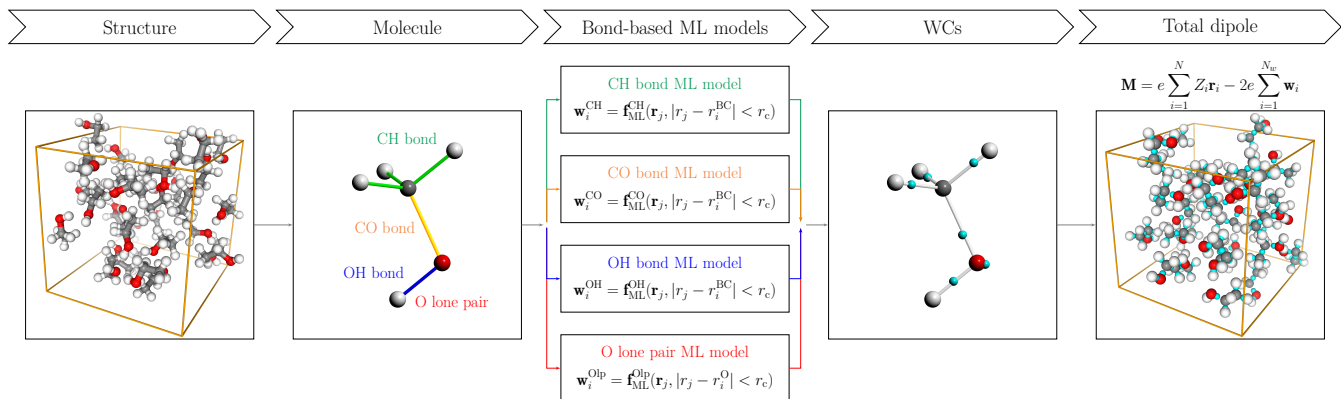


FIG. 3: Workflow to calculate the total dipole moment from bond-based ML dipole models. We create ML models for each bond species to predict the WC assigned to the bond. Predicting all WCs in the system, we obtain the total dipole moment according to Eq. (1).

ion-core part can be calculated from ion-core charges and positions as usual, whereas the valence-electronic contribution is evaluated from the $-2e$ point charges at i -th WC \mathbf{w}_i as

$$\mathbf{M} = \mathbf{M}_{\text{atom}} + \mathbf{M}_{\text{el}} = e \sum_{i=1}^N Z_i \mathbf{r}_i - 2e \sum_{i=1}^{N_w} \mathbf{w}_i, \quad (1)$$

where Z_i is the ion-core charge of atoms, and \mathbf{r}_i denotes the nuclear position. N and N_w are the number of atoms and WCs, respectively. The coefficient of -2 comes from the degeneracy of spin degrees of freedom. We use a valence-only pseudopotential approach so that the WCs correspond to the valence electrons, and ion-core charges eZ_i are the sums of the charges of the bare nuclei and the frozen core electrons.

Our central idea is to rewrite Eq. (1) into a chemical bond-based expression. We assume that WCs are close enough to the centers of chemical bonds, called bond centers (BCs), or ion-cores in case of electron lone pairs, so that each WC can be clearly allocated to the corresponding BC or ion-core one by one, which is true in ordinary molecular systems. The examples of methanol and ethanol, shown in Fig. 1, illustrates that the WCs are well localized on the chemical bonds or the O lone pairs.

To clarify the discussion, we consider the system composed of oxygens, carbons, and hydrogens with single bonds and oxygen lone pairs in this paper. The extension to systems with double bonds or triple bonds is straightforward. We can associate each WC with a specific chemical bond or a lone pair, i.e., a single bond has one WC at \mathbf{w}^s , and an oxygen atom has two lone pair WCs at \mathbf{w}^{lp_1} and \mathbf{w}^{lp_2} . Therefore, the electronic term in Eq. (1)

can be recast to the bond-based form as

$$\mathbf{M}_{\text{el}} = -2e \sum_{i=1}^{N_{\text{single}}} \mathbf{w}_i^s - 2e \sum_{i=1}^{N_{\text{lp}}} \left(\mathbf{w}_i^{\text{lp}_1} + \mathbf{w}_i^{\text{lp}_2} \right) \quad (2)$$

$$= -2e \sum_{i=1}^{N_{\text{single}}} \mathbf{w}_i^s - 4e \sum_{i=1}^{N_{\text{lp}}} \mathbf{w}_i^{\text{lp}}, \quad (3)$$

where N_{single} and N_{lp} are the number of single bonds and lone pairs, respectively. N_{lp} is also identical to the number of oxygen atoms in our case. $\mathbf{w}_i^{\text{lp}} = (\mathbf{w}_i^{\text{lp}_1} + \mathbf{w}_i^{\text{lp}_2})/2$ is the center of mass of two lp WCs. Henceforth, we also treat \mathbf{w}_i^{lp} as WCs. Equation (3) is the most important equation, representing the one-to-one correspondence between each chemical bond (or lp) and WCs.

To further simplify the equation, we devise a similar decomposition for the ion-core term in Eq. (1). A carbon atom has four bonds, a hydrogen atom has one bond, and an oxygen atom has one bond and two lone pairs. Considering that atoms supply the associated single bonds with $+e$ charge and lone pairs with $+2e$ charges, we can also express the atomic contribution in Eq. (1) in the bond-based form as

$$\mathbf{M}_{\text{ion}} = e \sum_{i=1}^{N_{\text{single}}} (\mathbf{r}_i^1 + \mathbf{r}_i^2) + 4e \sum_{i=1}^{N_{\text{lp}}} \mathbf{r}_i^{\text{O}} \quad (4)$$

$$= 2e \sum_{i=1}^{N_{\text{single}}} \mathbf{r}_i^s + 4e \sum_{i=1}^{N_{\text{lp}}} \mathbf{r}_i^{\text{O}}, \quad (5)$$

where \mathbf{r}_i^λ ($\lambda = 1, 2$) denotes the atomic position associated with the bond i , and $\mathbf{r}_i^s = (\mathbf{r}_i^1 + \mathbf{r}_i^2)/2$ are the BCs. \mathbf{r}_i^{O} is the position of the oxygen i . Adding Eq. (2) and (4), we finally reach the bond-based expression of

the total dipole moment as

$$\mathbf{M} = 2e \sum_{i=1}^{N_{\text{single}}} (\mathbf{r}_i^s - \mathbf{w}_i^s) + 4e \sum_{i=1}^{N_{\text{lp}}} (\mathbf{r}_i^{\text{O}} - \mathbf{w}_i^{\text{lp}}) \quad (6)$$

$$= \sum_{i=1}^{N_{\text{single}}} \boldsymbol{\mu}_i^{\text{single}} + \sum_{i=1}^{N_{\text{lp}}} \boldsymbol{\mu}_i^{\text{lp}}. \quad (7)$$

We call $\boldsymbol{\mu}_i^{\text{single}} = 2e(\mathbf{r}_i^s - \mathbf{w}_i^s)$ and $\boldsymbol{\mu}_i^{\text{lp}} = 4e(\mathbf{r}_i^{\text{O}} - \mathbf{w}_i^{\text{lp}})$ bond dipoles, which are just the relative vectors from BCs (or oxygens) to WCs, as shown in Fig. 2. In the following, we equate bond dipoles with WCs. Equation (7) shows that the total dipole moment is decomposed into bond and lone pair components. Therefore, with ML models that predict the bond dipole for each bond and lone pair from neighboring atomic coordinates $\{\mathbf{R}\}$ as $\boldsymbol{\mu} = \mathbf{f}(\{\mathbf{R}\})$, we can infer the total dipole moments, as shown in Fig. 3.

B. Model Construction

We construct a neural network vector function \mathbf{f} that predicts the bond dipole $\boldsymbol{\mu}_i$, given the coordinates of the neighborhood atoms $\mathbf{r}_k \in N_i$ around the BC \mathbf{r}_i^s or lone pair atom \mathbf{r}_i^{O} within the cutoff radius r_c as $\boldsymbol{\mu}_i = \mathbf{f}(\{\mathbf{r}_k \in N_i\})$.

We followed the method proposed by Zhang et al. [67] so that \mathbf{f} satisfies the translational, permutational, and rotational symmetry. To preserve translational symmetry, we make a relative coordinate from a target BC \mathbf{r}_i^s or lone pair atom \mathbf{r}_i^{O} as $\mathbf{r}'_{ki} = \mathbf{r}_k - \mathbf{r}_i^s = (x_{ki}, y_{ki}, z_{ki})$ or $\mathbf{r}'_{ki} = \mathbf{r}_k - \mathbf{r}_i^{\text{O}} = (x_{ki}, y_{ki}, z_{ki})$, respectively. Then, we introduce the following cutoff function $s(r)$ as

$$s(r) = \begin{cases} \frac{1}{r} & r < r_{c0} \\ \frac{1}{r} \left\{ \frac{1}{2} \cos\left(\pi \frac{r-r_{c0}}{r_{c0}-r_c}\right) + \frac{1}{2} \right\} & r_{c0} < r < r_c \\ 0 & r_c < r. \end{cases} \quad (8)$$

We describe the atomic coordinates \mathbf{r}'_{ik} with a four component vector

$$\mathbf{q}_{ik} = (q_{ik}^1, q_{ik}^2, q_{ik}^3, q_{ik}^4) \quad (9)$$

$$= (s(r'_{ik}), s(r'_{ik})x'_{ik}, s(r'_{ik})y'_{ik}, s(r'_{ik})z'_{ik}). \quad (10)$$

The N_i by 4 matrix $\mathbf{Q} = (Q_{k\lambda}) = (q_{ik}^\lambda)$ represent the set of coordinates $\{\mathbf{q}_{ik}\}$ in a neighborhood, where λ is the Cartesian index. In the actual calculation, \mathbf{q}_{ik} are ordered by atomic species in ascending order with respect to r'_{ki} .

Next, we introduce two deep neural networks (DNN), an embedding DNN and a fitting DNN to ensure permutational invariance and rotational covariance. The embedding DNN $\mathbf{E}(\{s(r')\})$ is the mapping from the set $\{q_{ik}^\lambda | k = 1, \dots, N_i\}$ onto the matrix with M rows and N_i columns. To reduce the computational cost, we define the truncated embedding matrix \mathbf{E}' formed by the

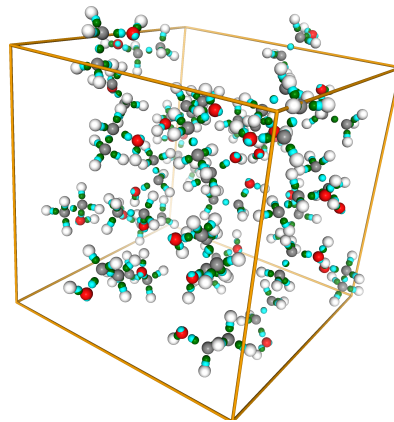


FIG. 4: Snapshot of MD simulation with ML dipole moments for liquid ethanol containing 32 molecules. The coordinates of the BCs (dark green) are computed at each MD step, and the ML models predict the WCs (light blue). Hydrogen, oxygen, and carbon atoms are shown in white, red, and gray, respectively.

embedding matrix's first $M' (< M)$ columns. Using \mathbf{E} and \mathbf{E}' , we construct the feature matrix \mathbf{D} of dimension $M \times M'$ as

$$\mathbf{D}_i = (\mathbf{E}\mathbf{Q})(\mathbf{E}'\mathbf{Q})^T = \mathbf{E}\mathbf{Q}\mathbf{Q}^T\mathbf{E}'^T. \quad (11)$$

In the feature matrix, translational and rotational symmetries are preserved by the matrix product of $\mathbf{Q}\mathbf{Q}^T$.

The fitting DNN $\mathbf{F}(\mathbf{D})$ maps \mathbf{D}_i onto M outputs $F_j (j = 1, 2, \dots, M)$, which are finally used to calculate $\boldsymbol{\mu}_i = (\mu_i^1, \mu_i^2, \mu_i^3)$ with the last three columns of $\mathbf{T} = \mathbf{E}\mathbf{Q}$,

$$\mu_i^\lambda = \sum_{j=1}^M F_j(\mathbf{D})T_{j,\lambda+1} \quad (\lambda = 1, 2, 3). \quad (12)$$

We define the loss function as

$$L = \frac{1}{n_b} \sum_{i=1}^{n_b} |\boldsymbol{\mu}_i^{\text{p}} - \boldsymbol{\mu}_i^{\text{t}}|^2, \quad (13)$$

where $\boldsymbol{\mu}_i^{\text{p}}$ and $\boldsymbol{\mu}_i^{\text{t}}$ are the predicted and DFT bond dipole moments of the i -th data, respectively, and n_b is the batch size. We train different ML models for each chemical bond species according to Eq. (13).

C. The dielectric properties

The dielectric function at angular frequency ω of the external electric field is a complex quantity written as

$$\varepsilon(\omega) = \varepsilon'(\omega) - i\varepsilon''(\omega), \quad (14)$$

where ε' and ε'' are the real and imaginary parts, respectively. We consider the relative dielectric function, and all ε are dimensionless. From the linear response theory,

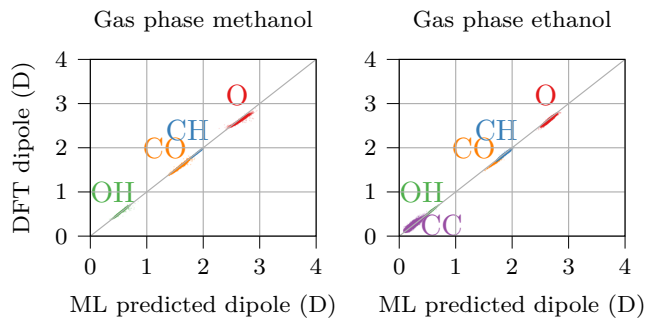


FIG. 5: Learning accuracy of ML dipole models for gas phase (left) methanol and (right) ethanol, where the x -axis represents the value predicted by ML and the y -axis represents the value calculated by DFT. There are four models for methanol and five for ethanol. The data are taken from both training and test data. The blue, orange, green, red, and purple dots represent the absolute values of the CH, CO, OH, O, and CC bond dipole moments, respectively.

TABLE I: RMSE [D] of ML dipole models for methanol and ethanol, calculated from validation data. The CC bond model exists only for ethanol.

RMSE [D]	gas		liquid	
	methanol	ethanol	methanol	ethanol
CC	-	0.035	-	0.040
CH	0.004	0.011	0.030	0.029
CO	0.011	0.030	0.023	0.029
OH	0.010	0.008	0.022	0.024
O	0.023	0.020	0.040	0.040

the dielectric function $\varepsilon(\omega)$ of an isotropic and homogeneous fluid in MD simulations with periodic boundary conditions is given by [70–73]

$$\varepsilon(\omega) = \varepsilon^\infty - \frac{1}{3k_B T} \int_0^\infty \left(\frac{d \langle \tilde{\mathbf{M}}(0) \cdot \tilde{\mathbf{M}}(t) \rangle}{dt} \right) e^{-i\omega t} dt, \quad (15)$$

where $\langle \rangle$ denote the canonical ensemble averages, and $\tilde{\mathbf{M}}(t) = \mathbf{M}(t) - \langle \mathbf{M} \rangle$ is the zero-mean dipole moment along a MD trajectory. ε^∞ is the high-frequency dielectric constant, k_B is the Boltzmann constant, T is the temperature, and V is the volume of the simulation cell. Using the static dielectric constant

$$\varepsilon^0 = \varepsilon(0) = \varepsilon^\infty + \frac{1}{3k_B T V} \left(\langle \mathbf{M}^2 \rangle - \langle \mathbf{M} \rangle^2 \right), \quad (16)$$

we rewrite Eq. (15) as

$$\frac{\varepsilon(\omega) - \varepsilon^\infty}{\varepsilon^0 - \varepsilon^\infty} = \int_0^\infty \left(-\frac{d\Phi(t)}{dt} \right) e^{-i\omega t} dt, \quad (17)$$

where $\Phi(t)$ is the Fourier transform of the normalized autocorrelation function of the dipole moment $\tilde{\mathbf{M}}(t)$,

$$\Phi(t) = \frac{\langle \tilde{\mathbf{M}}(0) \cdot \tilde{\mathbf{M}}(t) \rangle}{\langle \tilde{\mathbf{M}}^2 \rangle}. \quad (18)$$

To avoid evaluating the derivative of the auto-correlation function, we adopt the alternative form derived from the integration by parts of Eq. (17) [74]

$$\frac{\varepsilon(\omega) - \varepsilon^\infty}{\varepsilon^0 - \varepsilon^\infty} = 1 - i\omega \int_0^\infty \Phi(t) e^{-i\omega t} dt. \quad (19)$$

The complex refractive index $\hat{n}(\omega)$ is another important optical quantity defined as

$$\hat{n}(\omega) = n(\omega) - i\kappa(\omega), \quad (20)$$

where the real part $n(\omega)$ is the refractive index, and the imaginary part $\kappa(\omega)$ is the optical extinction coefficient. The complex dielectric constant and the complex refractive index are related as

$$\varepsilon(\omega) = \hat{n}(\omega)^2. \quad (21)$$

Therefore, the imaginary part of the dielectric function is

$$\varepsilon''(\omega) = 2n(\omega)\kappa(\omega). \quad (22)$$

Absorption coefficient per unit length $\alpha(\omega)$ is defined through Lambert-Beer's law [75]:

$$\alpha(\omega) = \frac{2\omega}{c} \kappa(\omega), \quad (23)$$

where c is the speed of light in vacuum. Absorption spectrum $\alpha(\omega)n(\omega)$ is associated with $\varepsilon''(\omega)$ via the equation

$$\alpha(\omega)n(\omega) = \frac{2\omega k(\omega)}{c} n(\omega) = \frac{\omega}{c} \varepsilon''(\omega). \quad (24)$$

To analyze the spectra, we write the total dipole moment as the aggregate of the N individual molecular dipole moments, $\mathbf{M}(t) = \sum_{i=1}^N \boldsymbol{\mu}_i^{\text{mol}}(t)$, where $\boldsymbol{\mu}_i^{\text{mol}}(t)$ is the dipole moment of the i -th molecule. Then, the autocorrelation function appearing in Eq. (15) can be decomposed as

$$\begin{aligned} \langle \mathbf{M}(0) \cdot \mathbf{M}(t) \rangle &= \sum_{i=1}^N \langle \boldsymbol{\mu}_i^{\text{mol}}(0) \cdot \boldsymbol{\mu}_i^{\text{mol}}(t) \rangle \\ &+ \sum_{i \neq j} \langle \boldsymbol{\mu}_i^{\text{mol}}(0) \cdot \boldsymbol{\mu}_j^{\text{mol}}(t) \rangle. \end{aligned} \quad (25)$$

The first term is the autocorrelations of the dipole moments of single molecules, and the second is cross-correlations among the dipole moments of different molecules [47]. Substituting Eq. (25) into Eq. (15), we

acquire the self and collective component of the absorption as

$$\varepsilon''_{\text{self}}(\omega) = -\frac{1}{3k_{\text{B}}T} \int_0^\infty \frac{d}{dt} \left(\sum_{i=1}^N \langle \boldsymbol{\mu}_i^{\text{mol}}(0) \cdot \boldsymbol{\mu}_i^{\text{mol}}(t) \rangle \right) e^{-i\omega t} dt, \quad (26)$$

$$\varepsilon''_{\text{coll}}(\omega) = -\frac{1}{3k_{\text{B}}T} \int_0^\infty \frac{d}{dt} \left(\sum_{i \neq j} \langle \boldsymbol{\mu}_i^{\text{mol}}(0) \cdot \boldsymbol{\mu}_j^{\text{mol}}(t) \rangle \right) e^{-i\omega t} dt, \quad (27)$$

yielding

$$\alpha(\omega)n(\omega) = \frac{\omega}{c} \varepsilon''_{\text{self}}(\omega) + \frac{\omega}{c} \varepsilon''_{\text{coll}}(\omega). \quad (28)$$

D. The velocity auto-correlation function

The velocity auto-correlation function (VACF) of atom i is defined as

$$v_i^{\text{ACF}}(t) = \langle \mathbf{v}_i(0) \cdot \mathbf{v}_i(t) \rangle, \quad (29)$$

where $\mathbf{v}_i(t)$ is the atomic velocity at time t . The total VACF is the average of atomic VACF as

$$V^{\text{ACF}}(t) = \frac{1}{N} \sum_{i=1}^N v_i^{\text{ACF}}(t), \quad (30)$$

where N is the number of atoms in the system. We can calculate the VACF for each atomic species by restricting the summation. The vibrational density of states is the Fourier transformation of VACF as

$$D(\omega) = \int_{-\infty}^{\infty} V^{\text{ACF}}(t) e^{-i\omega t} dt, \quad (31)$$

which gives the spectral information of atomic movements.

The angular velocity auto-correlation function of atom i belonging to molecule a , defined as

$$\omega_i^{\alpha, \text{ACF}}(t) = \langle \omega_i^\alpha(0) \omega_i^\alpha(t) \rangle, \quad (32)$$

represents the intramolecular rotational motions, where α is the Cartesian index. $\boldsymbol{\omega}_i(t)$ is the atomic angular velocity at time t , which can be calculated from the relative angular momentum $\mathbf{L}_i(t)$ of atom i from the center of mass of the molecule a and the inertia tensor I_a of the molecule a as

$$\mathbf{L}_i(t) = I_a(t) \boldsymbol{\omega}_i(t). \quad (33)$$

The eigenvectors $\mathbf{e}_a^\alpha(t)$ and eigenvalues $I_a^\alpha(t)$ of the inertia tensor are called the principal axes of inertia and principal moments of inertia, respectively. The three principal axes of inertia are frequently used as instantaneous molecular coordinates [4, 24]. In this frame, the angular

velocity is simply the angular momentum divided by the principal moment of inertia. By analogy with Eq. (31), the Fourier transform of Eq. (32) gives the spectrum of the rotational motion of the molecules:

$$D^\alpha(\omega) = \int_{-\infty}^{\infty} \frac{1}{N} \sum_{i=1}^N \omega_i^{\alpha, \text{ACF}}(t) e^{-i\omega t} dt. \quad (34)$$

III. RESULTS AND DISCUSSION

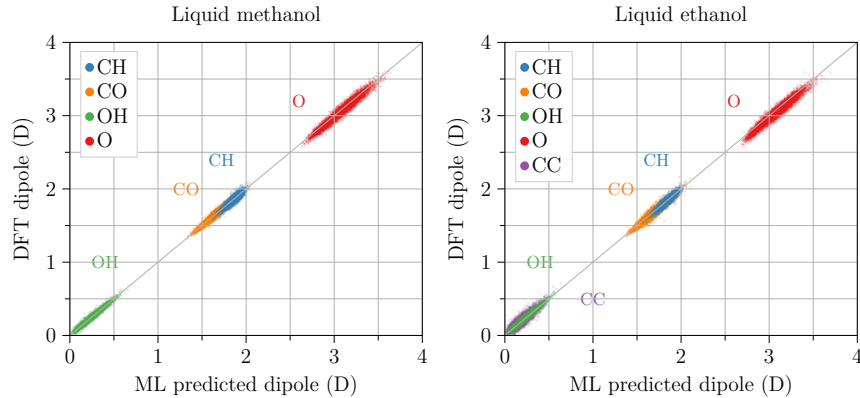
A. Computational details

We used the CPMD package [79] to compute the electronic ground state, BOMD calculations, and WCs. The Becke-Lee-Yang-Parr (BLYP) functional [80, 81] within the generalized gradient approximation (GGA) framework with Grimme's dispersion correction D2 [82] was used for the exchange-correlation functional, and the Goedecker-Teter-Hutter (GTH) pseudopotentials [83] was employed with the plane wave cutoff of 100 Ry. The BLYP functional has been used regularly in past AIMD simulations of methanol [34–36, 38, 39, 41, 42, 44]. The energy convergence conditions were $1 \times 10^{-7} E_{\text{h}}$ for the ML training data and $1 \times 10^{-4} E_{\text{h}}$ for the BOMD calculations. Only Γ point was used in the electron density integration. Lattice constants were determined from experimental densities [76] for liquid simulations with 48 molecules for methanol and 32 for ethanol, while they were fixed at 20 Å for gas phase calculations.

We employed the CMD calculations with the GRO-MACS package [84] to prepare ML training structures and initial configurations for the AIMD simulations. The general AMBER force field (GAFF2) [85] and the AM1-BCC charge [86] were used. Topology files were generated by the Antechamber package [87] and the ACPYPE package [88]. Initial systems were made by randomly placing molecules using the Packmol package [89] with the density fixed to the experimental values. The simulations were performed in an NVT ensemble at 300 K using velocity rescaling. The MD time step was 1 fs. Ten thousand training data structures for each material were sampled every 1 ps so that each structure was as uncorrelated as possible for both gas and liquid phases.

Calculated WCs were assigned to each chemical bond by accommodating the closest WC to each BC. Embedding and fitting ML models, coded using the Pytorch library [90], contain three hidden layers with 50 nodes. We chose the ReLU function [91] as the activation function for all hidden layers. The hyperparameters were set to $M = 20$ and $M' = 6$ to balance computation time and accuracy. The cutoffs for the descriptors were set to 4 Å for the inner cutoff and 6 Å for the outer cutoff. The Adam stochastic gradient descent method [92] was adopted for the optimization, where a mini-batch learning scheme with a batch size of 32 was used. We independently trained the ML models for methanol and ethanol,

(a) Bond dipole moment



(b) Molecular dipole moment

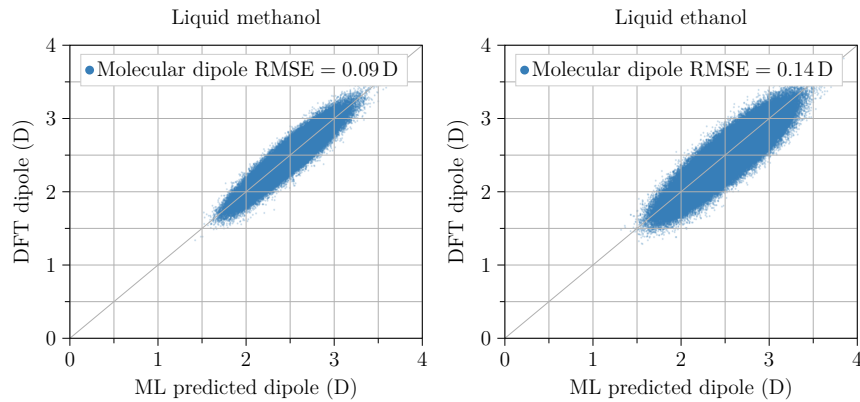


FIG. 6: (a) Learning accuracy of the bond dipole moments of (left) methanol and (right) ethanol, where the x -axis represents the value predicted by ML and the y -axis represents the value calculated by DFT. 10000 validation data are plotted. (b) Learning accuracy of the molecular dipole moments calculated from from the bond dipole model for liquid methanol and ethanol.

TABLE II: Molecular dipole moments μ^{mol} and dielectric constants ϵ^0 for methanol and ethanol obtained from

CMD and AIMD calculations at 298 K accompanied with experimental data of the gas phase dipole moment, dielectric constant, refractive index n , and density ρ . $\mu_{\text{G}}^{\text{mol}}$ and $\mu_{\text{L}}^{\text{mol}}$ are the average dipole moments calculated from gas and liquid models, respectively, from the hundred thousand molecular structures sampled from a 10 ps BOMD trajectory. $\Delta\mu^{\text{mol}} = \mu_{\text{L}}^{\text{mol}} - \mu_{\text{G}}^{\text{mol}}$ is the difference between liquid and gas calculations. Dipoles are in Debye and densities are in g/cm^3 .

	BOMD			CMD	Experiment			
	$\mu_{\text{G}}^{\text{mol}}$	$\mu_{\text{L}}^{\text{mol}}$	$\Delta\mu^{\text{mol}}$	ϵ^0	$\mu_{\text{G}}^{\text{mol}}$	ϵ^0	n	ρ
Methanol	1.72	2.69	0.97	33.0	1.70 [76]	32.66 [77]	1.329	0.7863 [78]
Ethanol	1.78	2.71	0.93	21.2	1.69 [76]	24.43 [77]	1.361	0.7849 [78]

gas and liquid phases. The code is implemented in the MLWC (machine learning Wannier center) package [93].

BOMD simulations combined with ML dipole moments were carried out to calculate dielectric properties. After initial configurations were generated from 10 ns CMD calculations, we performed a 5 ps equilibration run by BOMD, from which production runs of 10 ps were carried out. All the BOMD simulations were conducted in an NVT ensemble at 300 K with a Nosé-Hoover

thermostat, with the integration time step of 0.25 fs.

As the estimation of ϵ^∞ was not within the scope of this work, we evaluated it from the square of the refractive index n as $\epsilon^\infty = n^2$. The experimental values [76] of $n = 1.329$ for methanol and $n = 1.361$ for ethanol at 298 K were used, noting that the temperature dependence of the refractive index is small.

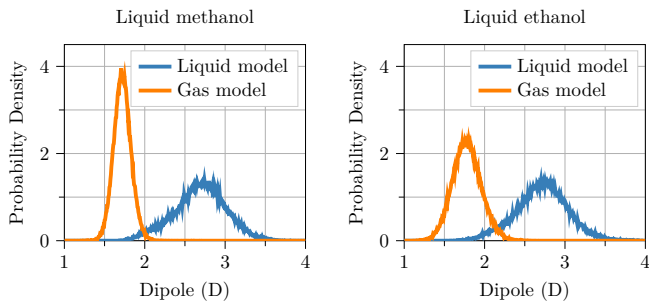


FIG. 7: Molecular dipole moments of (left) methanol and (right) ethanol in the liquid phase predicted from gas models (orange) and liquid models (blue). Hundred thousand molecules are randomly sampled from 10 ps BOMD calculations.

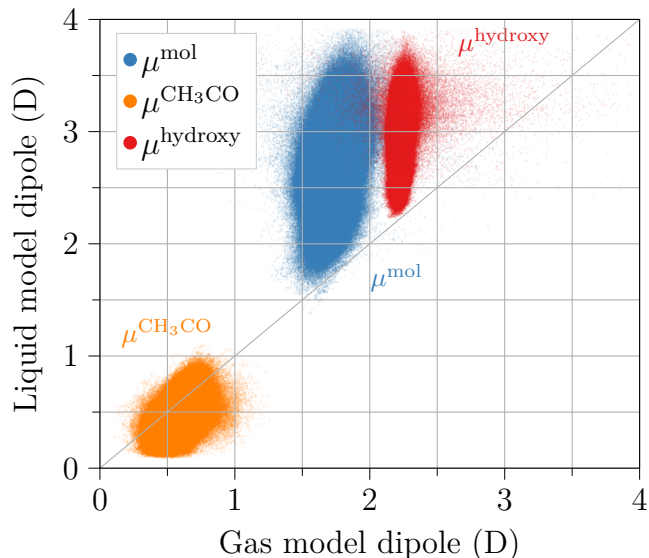


FIG. 8: Calculated bond dipole moments of $\mu^{\text{CH}_3\text{CO}} = \mu^{\text{CH}_3} + \mu^{\text{CO}}$ (orange), $\mu^{\text{hydroxy}} = \mu^{\text{OH}} + \mu^{\text{Olp}}$ (red), and μ^{mol} (blue). The x and y axes represent the predictions by the gas and liquid models, respectively. Hundred thousand molecules are randomly sampled from 10 ps BOMD calculations.

B. Model accuracy for gas phase

We have four ML dipole models for methanol, namely the CH bond, CO bond, OH bond, and O lone-pair (O-lp) models, whereas there is an additional CC bond model for ethanol. We first discuss the results of the isolated (gas phase) methanol and ethanol. Figure 5 compares dipole moments calculated from first principles with those predicted by the ML models, showing excellent agreement with each other. As there is no polarization owing to intermolecular interactions in isolated systems, ML models only need to learn the effect of intramolecular deformations on the displacement of the WCs. We note that the inner cutoff of 4 Å for the de-

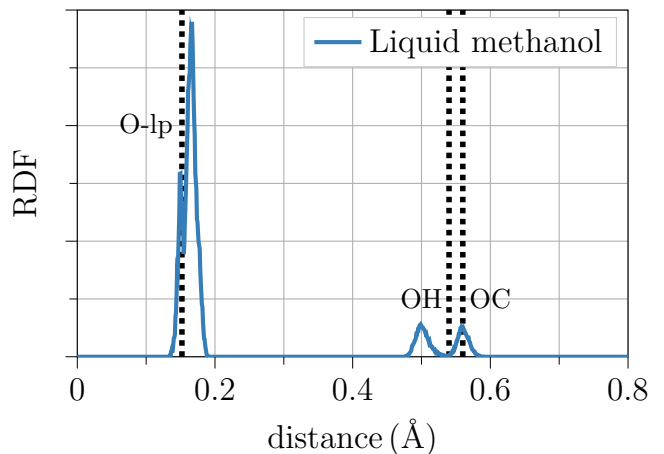


FIG. 9: The radial distribution function from O atoms to WCs in liquid methanol. In the case of a lone pair, it is the center of gravity of the two WCs. The three peaks correspond to the O lone pair, the second to the WCs of the OH bond, and the third to the WCs of the OC bond, in increasing order of distance. The vertical lines indicate the peak positions in the gas phase.

scriptor is sufficiently large that the descriptors include all atoms. Table I summarizes the root mean square error (RMSE) of each model, defined as

$$\text{RMSE} = \sqrt{\frac{1}{n} \sum_{i=1}^n |\mu_i^p - \mu_i^t|^2}, \quad (35)$$

where n is the number of data. All ML models perform well with an accuracy of almost $\text{RMSE} = 0.03$ D or less, noting that the bond dipole moment of 1 D corresponds to about 0.1 Å of the displacement of WC.

C. Model accuracy for liquid phase

We next discuss the results for liquid systems. Intermolecular interactions cause significant polarization in liquids, which makes prediction more difficult. Figure 6 compares dipole moments calculated from first principles with those predicted by the ML models, showing good agreement with each other. Table I summarizes the RMSE of each model, with errors cured to less than 0.04 D. The O-lp model is the least accurate for methanol and ethanol in common because the WCs of the O-lp frequently move in liquids due to the electric field created by the surrounding molecules. Therefore, the prediction accuracy of the dipole moments of the system is sensitive to that of the O-lp.

Figure 6 also shows the prediction accuracy of the molecular dipole moments of liquid methanol and ethanol. For example, the dipole moments of methanol molecules are the sum of the corresponding bond dipole

TABLE III: Calculated dielectric constant of liquid methanol at 298 K using various ML models at 298 K with experimental data [77]. R stands for alkyl chains, CH₃ for methanol and CH₃CO for ethanol. The superscripts G and L represent the predicted values by the gas and liquid models.

	gas	R ^L + OH ^G + Olp ^G	R ^G + OH ^L + Olp ^L	liquid	Exp. [77]
Methanol	14.1	18.1	26.7	33.0	32.66
Ethanol	8.59	10.8	18.3	21.2	24.43

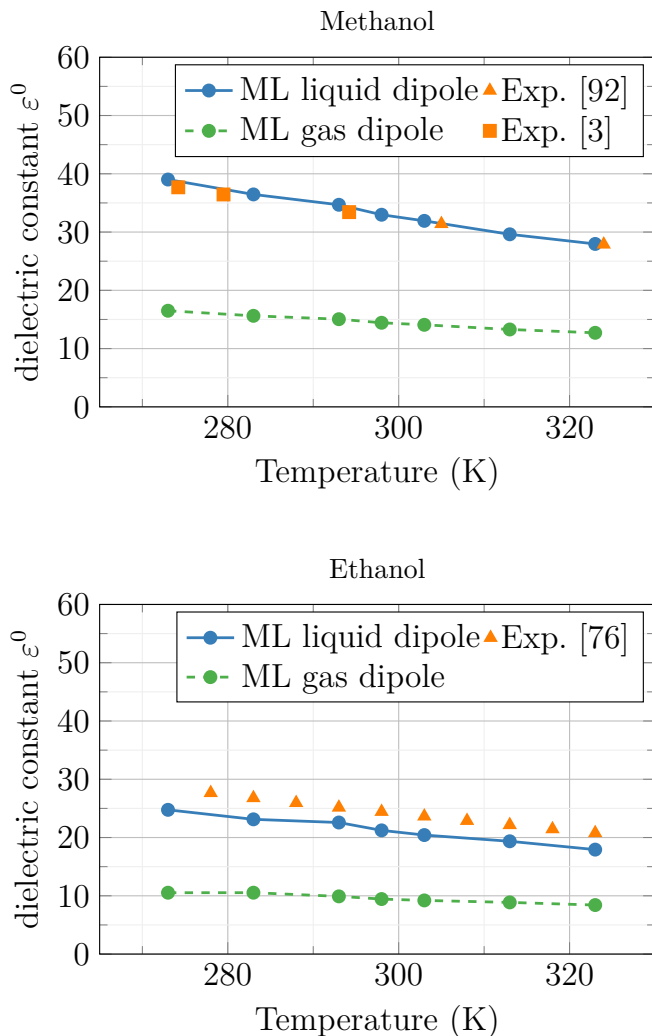


FIG. 10: Temperature dependence of the dielectric constant of methanol (top) and ethanol (bottom) calculated from liquid (blue) and gas (green) models using 50 ns CMD trajectories. The experimental values (orange) are taken from Refs [3, 77, 94].

moments using Eq. (7) as

$$\boldsymbol{\mu}^{\text{mol}} = \boldsymbol{\mu}^{\text{Olp}} + \boldsymbol{\mu}^{\text{OH}} + \boldsymbol{\mu}^{\text{CO}} + \boldsymbol{\mu}_1^{\text{CH}} + \boldsymbol{\mu}_2^{\text{CH}} + \boldsymbol{\mu}_3^{\text{CH}}. \quad (36)$$

The RMSE for the methanol molecular dipole moments is 0.09 D and that for ethanol is 0.14 D, which are very ac-

curate given that the average molecular dipole moments are about 2.5 D for both materials.

The largest differences between isolated and liquid systems appear in the O-lp and OH models, which can be understood from the presence of hydrogen bonding in liquids. The O-lp dipole moments, which averaged about 2.8 D in the gas phase, increase to 3.7 D in the liquid phase, and the dipole moments of the OH bonds, which averaged about 0.5 D in the gas phase, take values ranging from 0 D to 1 D. Additionally, the O-lp dipole moments are most broadly distributed, indicating that the effect of the surrounding molecules can significantly change the positions of WCs. In contrast, the values of the CO, CH, and CC dipole moments vary slightly from the gas phase, suggesting that the WCs of these bonds are insusceptible to neighbor molecules.

D. The dipole moments

We utilized the gas and liquid ML models to examine the effect of intermolecular interactions in liquids on dipole moments. Figure 7 compares the molecular dipole moments of liquid molecular structures predicted from both gas (orange) and liquid (blue) models, where 1000 molecular structures were randomly sampled from the 10 ps BOMD trajectory at 300 K. The average molecular dipole moments from liquid models were approximately 1 D larger than those from gas models in both methanol and ethanol, as in previous studies [2, 34]. Since the molecular structures are taken from simulated liquids, the difference entirely stems from the polarization of the WCs due to intermolecular interactions. Table II summarizes the average molecular dipole moments, where $\mu_{\text{G}}^{\text{mol}}$ and $\mu_{\text{L}}^{\text{mol}}$ stand for the dipole moments of the gas and liquid phases, respectively. Predicted values aligned well with experimental values [76] in the gas phase. For the liquid phase of methanol, previous DFT simulations using the same functional reported 2.54 D [34] or 2.68 D [43], which were consistent with our result of 2.69 D.

To examine which bond dipole moments have large difference between gas and liquid models, Fig. 8 compares the bond dipole distributions of $\boldsymbol{\mu}^{\text{CH}_3\text{CO}} = \boldsymbol{\mu}^{\text{CH}_3} + \boldsymbol{\mu}^{\text{CO}}$ (orange), $\boldsymbol{\mu}^{\text{hydroxy}} = \boldsymbol{\mu}^{\text{OH}} + \boldsymbol{\mu}^{\text{Olp}}$ (red), and $\boldsymbol{\mu}^{\text{mol}}$ (blue) calculated from both liquid and gas models using liquid methanol structures. We found that $\boldsymbol{\mu}^{\text{hydroxy}}$ is significantly enhanced in liquid models, while $\boldsymbol{\mu}^{\text{CH}_3\text{CO}}$ shows

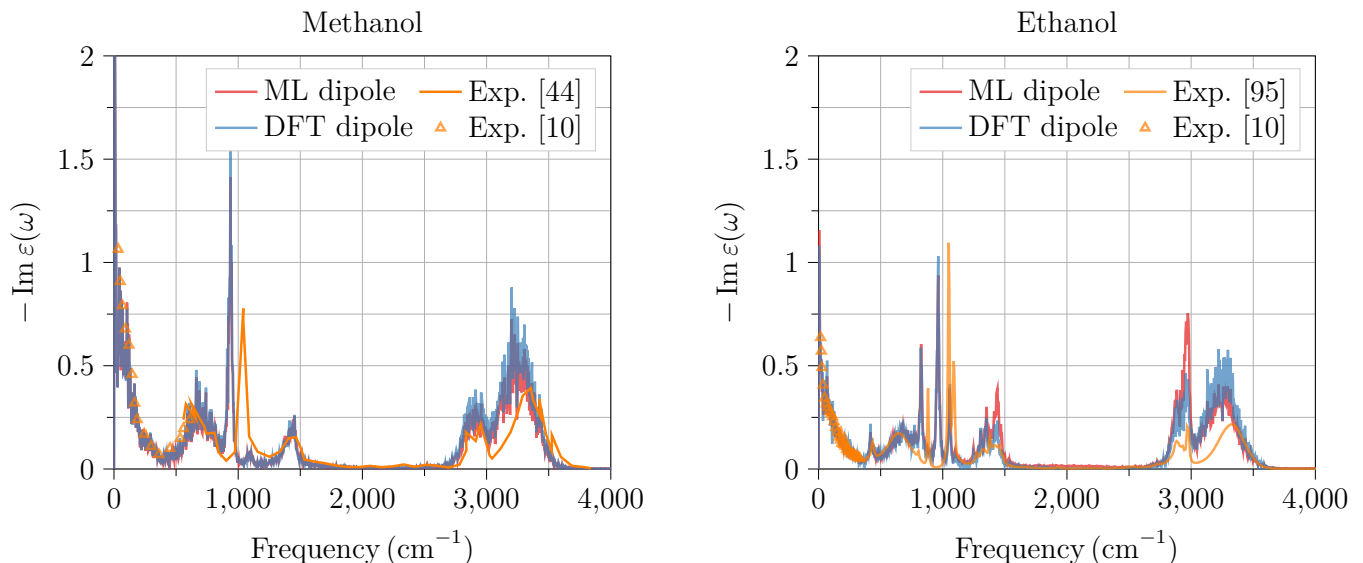


FIG. 11: Calculated imaginary part of dielectric functions of methanol (left) and ethanol (right) accompanied by experimental values (orange) [10, 44, 95] at room temperature. All trajectories utilized 10 ps BOMD calculations and dipoles were calculated both from ML (red) and DFT (blue).

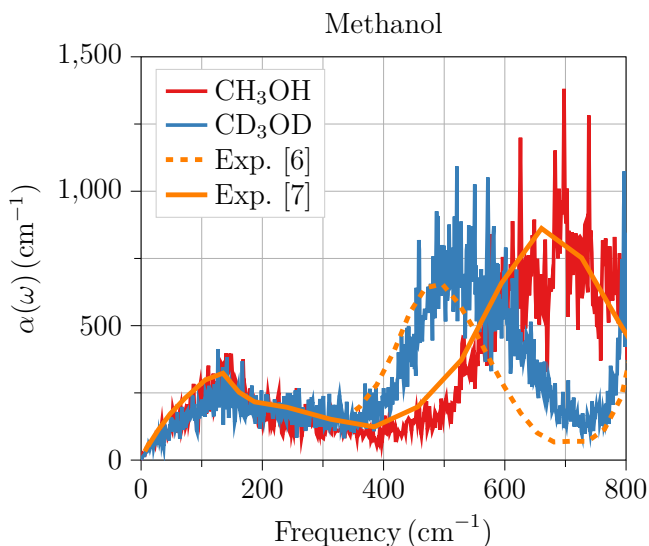


FIG. 12: Calculated absorption $\alpha(\omega)$ of methanol (red) and deuterated methanol (blue), which were computed with BOMD trajectories and ML dipole models. The experimental spectra of methanol (orange) [6] and deuterated methanol (orange dashed) [7] are also shown.

less variation.

Figure 9 shows the radial distribution function (RDF) from O atoms to WCs in liquid methanol. The three peaks correspond to the O lp, OH bond, and CO bond, in ascending order of distance. Comparing the peak positions in the liquid phase with those in the gas phase (vertical dotted lines), we found that the WCs of O lp move further away from the O atom, while the WCs of the OH bond move closer to the O atoms in the liquid

phases, as shown in previous studies [34, 96], thus increasing μ^{hydroxy} .

E. The dielectric constants

Since long trajectories are required to calculate dielectric constants [66], we performed 50 ns CMD calculations and predicted the dipole moment every 1 ps using 333 and 500 molecule systems for methanol and ethanol, respectively. The timescale is far beyond the DFT capacity. We used the experimental densities at each temperature [97] ranging from 273 K to 323 K to determine the lattice constants. We evaluated the static dielectric constants using Eq. (16), which does not contain dynamical information and requires only sufficient structural sampling at equilibrium for convergence. We achieved rapid structure sampling through CMD and accurate dipole moment calculations via ML models, accounting for intermolecular interaction effects.

Figure 10 shows that predicted dielectric constants using liquid models (blue) agree well with experimental data (orange) [3, 77, 94], while calculated values from the gas models (green) underestimate the dielectric constants by more than 50% for both methanol and ethanol, indicating the importance of WC polarization on the dielectric constant. Some classical empirical point charges are known to underestimate the dielectric constant of methanol [25], which may be attributed to a similar cause. Also, our models were able to be used over various temperatures and densities, even though they were trained on structures only at 300 K. Ethanol might exhibit greater sensitivity to the choice of force field because of its more complex structure than methanol, which po-

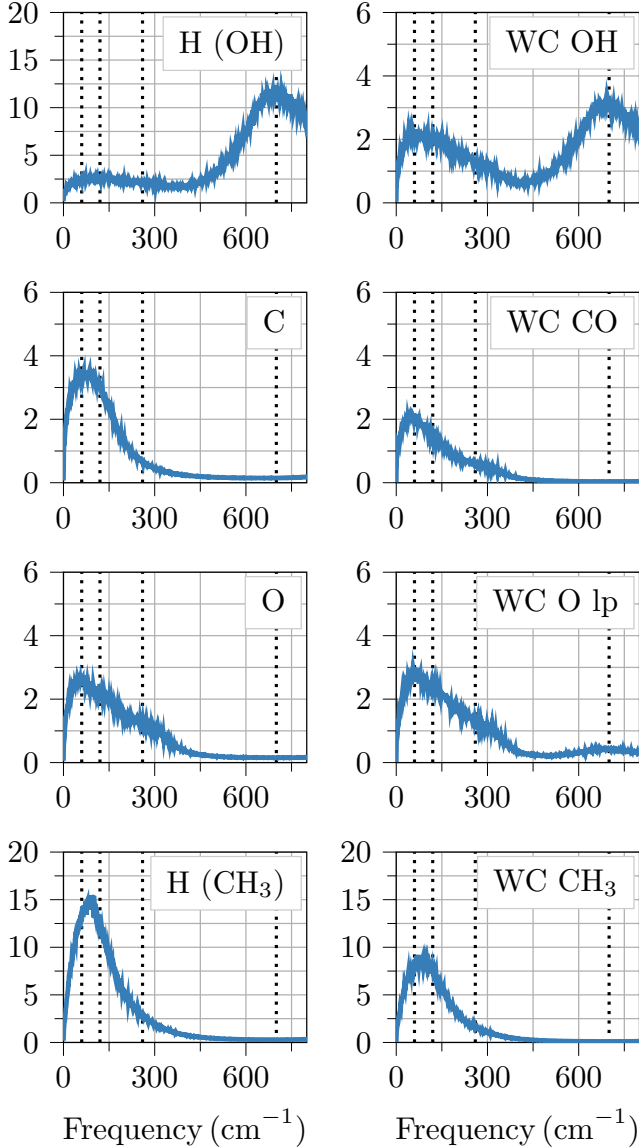


FIG. 13: Analysis of the vibrational density of states (VDOS) of liquid methanol. Each atomic and WC contributions are reported, where the hydroxyl hydrogen and the OH bond WC have a significant peak at 700 cm^{-1} . The vertical dotted lines represent experimentally observed peak positions at 60 , 120 , 260 , and 700 cm^{-1} .

tentially contributed to the underestimation of our calculations.

Table III summarizes the dielectric constants at 298 K calculated by the liquid models, gas models, and their combinations, where we divided the molecules into an alkyl chain and the hydroxy part (OH+Olp) and evaluated each part using the gas and liquid models. For methanol, the combination of the gas model evaluation for alkyl chains and liquid model calculation of the hydroxy part yields a dielectric constant of 26.7, which is close to the complete liquid calculation of 32.21. There-

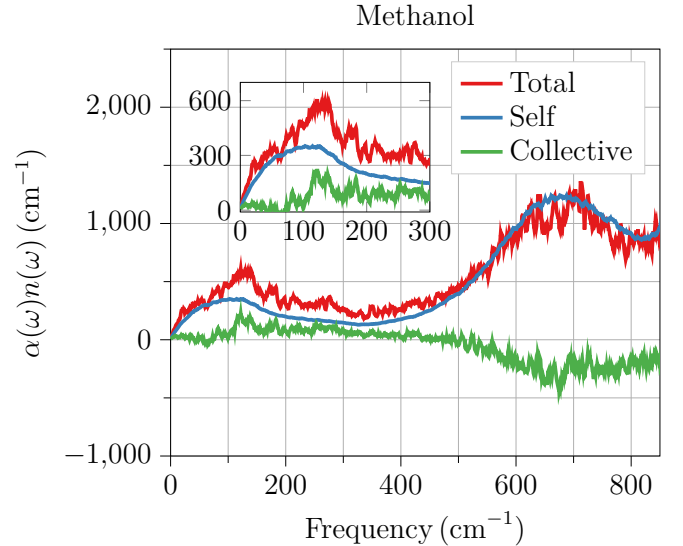


FIG. 14: Calculated absorption $\alpha(\omega)n(\omega)$ of methanol (red), decomposed into self (blue) and collective (green) components according to Eq. (28). We use the centered moving average method to smooth the spectra.

fore, the hydroxy part explains most of the dielectric constant, while the polarization of alkyl chains in liquids also has a non-negligible contribution. The same is true for ethanol.

F. The dielectric functions

Figure 11 shows the imaginary part of the dielectric function calculated from DFT (blue) and ML (red) in the IR region up to 4000 cm^{-1} , alongside experimental values (orange) at room temperature [10, 44, 98]. We averaged five independent BOMD trajectories of 10 ps to smooth the spectra, with the dipole moments evaluated using both DFT and ML models. Therefore, the difference between the ML and DFT calculations appears in the intensity of the spectra. Overall, ML results reproduced DFT calculations for both methanol and ethanol. Additionally, our calculations agree well with the experimental data, although some peaks show a redshift, which is characteristic of the BLYP functional [44]. Peak assignments have been done experimentally [99]: the 2900 cm^{-1} and 3300 cm^{-1} peaks are attributed to the stretching motion of CH and OH, respectively, while the 1300 cm^{-1} peak is ascribed to the bending of OH, and the peaks around 1000 cm^{-1} are of methyl groups motions.

To study THz spectra below 1000 cm^{-1} , we prepared five independent 20 ps BOMD trajectories with ML dipole moments. First, we focus on the libration peak at 700 cm^{-1} . Figure 12 shows that the absorption spectra of deuterated and normal methanol agree well with experimental values at 298 K [6, 7]. The 700 cm^{-1} peak of normal methanol is shifted to about 500 cm^{-1} in deuterated methanol, which verifies that the 700 cm^{-1} peak is

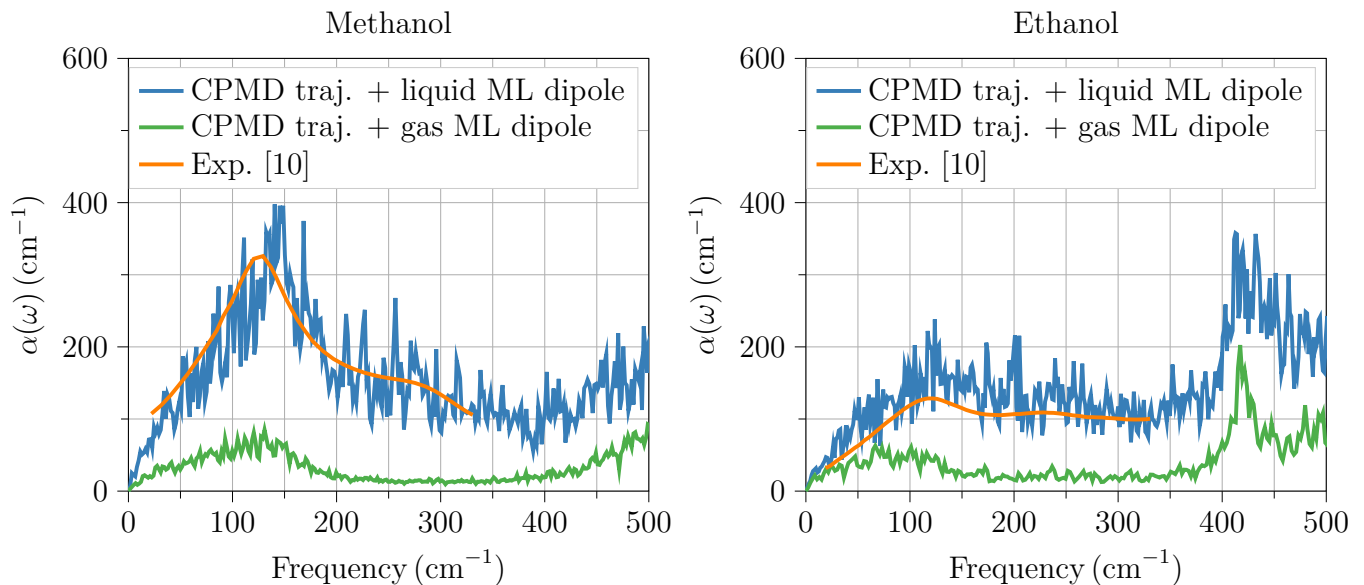


FIG. 15: Calculated absorption $\alpha(\omega)$ of methanol (left) and ethanol (right) from BOMD trajectories and ML dipole moments. The liquid model calculations (blue) agree well with experimental values (orange) at room temperature from Sarker et al. [10], while the gas model calculations (green) underestimate them.

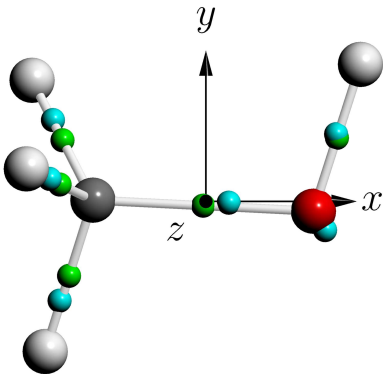


FIG. 16: Principal inertia axes of methanol. We define x , y , and z axes according to the decreasing order of their principal values.

due to hydrogen motions. In addition, Fig. 13 shows the partial VDOS of the atoms and WCs using Eq. (31), from which we found that the hydroxyl hydrogens and WCs exhibit a strong peak at 700 cm^{-1} . Therefore, the 700 cm^{-1} peak is due to the motion of hydrogens in the OH bond, as pointed out in previous studies [17, 24].

Figure 14 shows the decomposition of simulated $\alpha(\omega)n(\omega)$ into self (blue) and collective (green) components according to Eq. (28). The 700 cm^{-1} libration peak is mostly described by the self component, whereas the collective (intermolecular) and self (intramolecular) components have equal positive contributions up to 300 cm^{-1} .

Figure 15 demonstrates that the calculated absorption coefficient $\alpha(\omega)$ up to 500 cm^{-1} using liquid ML models (blue) excellently agrees with experimental values (or-

ange) [10]. In contrast, the gas model calculations (green) considerably underestimate the experimental data. The 426 cm^{-1} peak seen only in ethanol is due to the CCO bending [99]. Of the 60 , 120 , and 260 cm^{-1} peaks of methanol noted in previous studies [10, 11], the former two appear as one solid peak on the low-frequency side, while the highest peak is very broad. In addition, the gas model calculations partially reproduce the first peak and fail to reproduce the last broad peak. Therefore, internal molecular motions can partly explain the first two peaks, while the broad peak is entirely due to intermolecular interactions.

To analyze the intramolecular motions, we performed the principal axes analysis of the angular velocity ACF of methanol. As shown in Fig. 16, we define x , y , and z -axes according to the increasing order of its principal values. The x -axis is approximately parallel to the CO bond, while the y -axis is almost in the COH plane. The z -axis is an out-of-plane vector orthogonal to these. Figure 17 shows that the angular velocity ACFs in principal axes have four significant features: the peaks at 60 , 120 , and 700 cm^{-1} for y , z , and x components, respectively, and the large values on the x -axis in the low-frequency region below 300 cm^{-1} . The highest 700 cm^{-1} peak is due to the rotational motion of the hydroxyl H atom around the x -axis, consistent with the conclusion in Fig. 12 and Fig. 13. The 60 and 120 cm^{-1} peaks arise from the rotational motion of carbon, oxygen, and alkyl hydrogen around y and z -axes, respectively. For the latter, the phenomenon that the x -axis ACF of alkyl hydrogens takes large values at low frequencies, which has not been reported in previous rigid molecule calculations [16, 19], has little effect on the dielectric spectra, as it does not generate dipole moments.

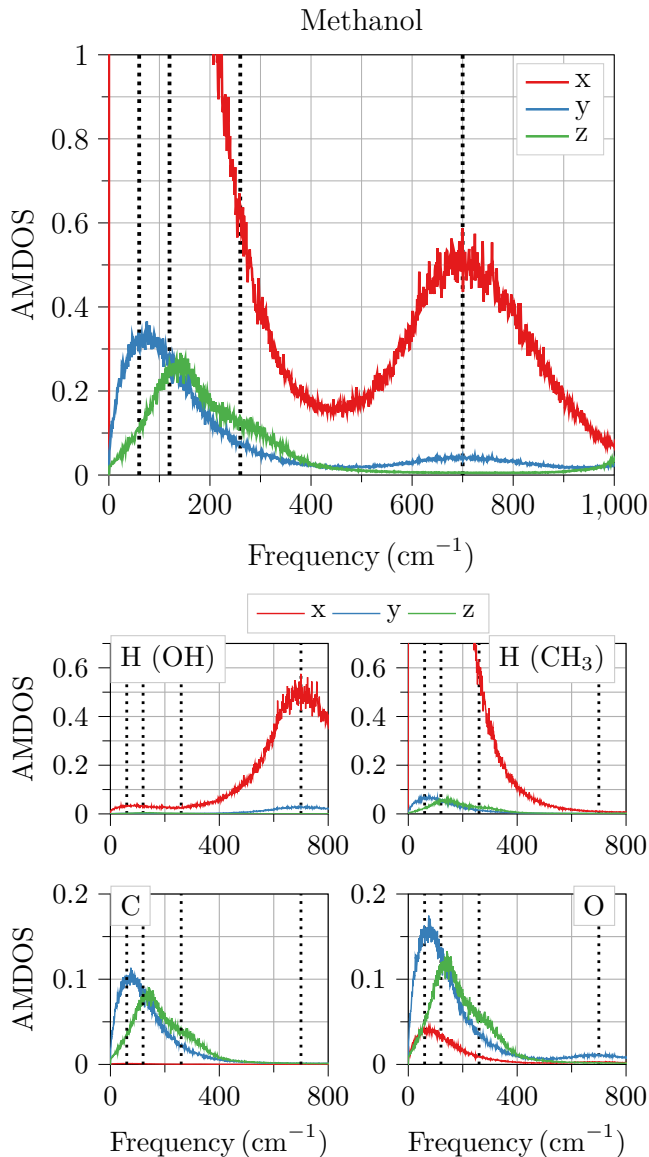


FIG. 17: Fourier spectra of the angular velocity auto-correlations around three principal axes of x (red), y (blue), and z (green) using Eq. (34). The full spectrum is displayed at the top, followed by the decomposition in terms of the atomic contributions.

The vertical dotted lines represent experimentally observed peak positions at 60, 120, 260, and 700 cm^{-1} . We use the centered moving average method to smooth the spectra.

In summary, the THz absorption spectrum of methanol is characterized by the libration peaks at 60 and 120 cm^{-1} , which are partially described by intramolecular vibrations, the libration peak at 700 cm^{-1} , which is almost completely described by intramolecular vibrations, and the broad peak at 260 cm^{-1} , which is completely described by intermolecular interaction. Alkyl hydrogen vibrations are also observed, but they do not significantly affect the dielectric properties.

IV. CONCLUSION

We have constructed a versatile ML scheme to predict dipole moments for molecular liquids by attributing WCs to each chemical bond and creating ML models that predict the WCs for each chemical bond. This scheme is applicable to any molecular system as long as the WCs can be assigned to chemical bonds. We applied the developed method to the primary alcohols methanol and ethanol, confirming its high accuracy in both the gas and liquid phases.

Using the developed method, we conducted the first-principles study on the dielectric properties of liquid methanol and ethanol. The dipole moment increases by approximately 1 D in the liquid phase compared to the gas phase, due to the WCs polarization of O-lp and OH bonds rather than the alkyl chains. The ML models, combined with CMD, accurately reproduced the experimental values of the dielectric constants. In contrast, the gas model calculations underestimate the dielectric constant by more than 50%. These results highlight the importance of the WCs polarization due to local intermolecular interactions.

The ML models were sufficiently accurate to calculate the IR dielectric function across the entire frequency range. The calculated THz absorption spectra also agreed well with the experiments. The 700 cm^{-1} peak was assigned to the libration motion of the hydroxyl hydrogen around the CO axis, as pointed out in previous studies [19, 24]. The low-frequency peaks were more complex, with approximately half of their magnitude resulting from intermolecular interactions. In particular, the broad 260 cm^{-1} peak was entirely due to intermolecular interactions. Intramolecular motions contribute to the out-of-plane (y -axis) librational peak at 60 cm^{-1} and the in-plane (z -axis) librational peak at 120 cm^{-1} . These analyses provide new insights into the origin of the THz spectrum of methanol and demonstrate the high accuracy of our ML models. We expect that the presented approach will be valuable for predicting the dielectric properties of a wide range of materials.

ACKNOWLEDGMENTS

This research was funded by a JST-Mirai Program Grant Number JPMJMI20A1, a MEXT Quantum Leap Flagship Program (MEXT Q-LEAP) grant number JPMXS0118067246, Japan, and JSR Corporation via JSR-UTokyo Collaboration Hub, CURIE. The computations in this study have been conducted using computational resources of the supercomputer Fugaku provided by the RIKEN Center for Computational Science (ProjectID: hp220331, hp230124) and the facility of the Supercomputer Center, the Institute for Solid State Physics, the University of Tokyo.

Appendix A: Linear response theory

To consider how to calculate the dielectric function in MD simulations, we start with the linear response theory of polarization $\bar{\mathbf{P}}(t)$ to an electric field $\mathbf{E}(t)$,

$$\bar{P}_\alpha(t) = \frac{1}{V} G^R(\hat{M}_\alpha, \hat{\mathbf{M}}, \omega) \cdot \mathbf{E}(t), \quad (\text{A1})$$

where V is the system volume, and $\hat{\mathbf{M}}$ is the dipole moment operator. α and β are the Cartesian indices. The retarded Green's function is given by

$$G^R(\hat{M}_\alpha, \hat{M}_\beta, \omega) = \int_0^\infty e^{-i\omega t} G^R(\hat{M}_\alpha(t), \hat{M}_\beta(0)) dt \quad (\text{A2})$$

$$G^R(\hat{M}_\alpha(t), \hat{M}_\beta(0)) = \frac{\theta(t)}{i\hbar} \left\langle \left[\hat{M}_\alpha(t), \hat{M}_\beta(0) \right] \right\rangle. \quad (\text{A3})$$

$\langle \rangle$ denotes the canonical ensemble average. Using the fact that the polarization and the electric field are connected by the dielectric susceptibility χ as $P_\alpha = \chi_{\alpha\beta} E_\beta$, and that the dielectric function in the IR region is the sum of the atomic contribution χ and the electron contribution ε^∞ as $\varepsilon_{\alpha\beta} = \varepsilon_{\alpha\beta}^\infty + \chi_{\alpha\beta}$, we write the dielectric function as

$$\varepsilon_{\alpha\beta}(\omega) = \varepsilon_{\alpha\beta}^\infty + \frac{1}{V} G^R(\hat{M}_\alpha, \hat{M}_\beta, \omega). \quad (\text{A4})$$

To utilize Eq. (A3) in the MD calculations, we must get the classical limit of the Green's function, where the dipole moment is just a number. We used the famous harmonic approximation [15, 100, 101], which replace the canonical correlation function [15] with classical correlation function. The canonical correlation of two operators A and B is defined as

$$\left\langle \hat{A}; \hat{B} \right\rangle_{\text{can}} = \frac{1}{\beta} \int_0^\beta d\lambda \left\langle e^{\lambda H_0} \hat{A} e^{-\lambda H_0} \hat{B} \right\rangle, \quad (\text{A5})$$

where H_0 is the unperturbed Hamiltonian and $\beta = 1/k_B T$ is the inverse temperature. To relate the canonical correlation with the retarded Green's function, we use the following equation

$$\left[\hat{A}, e^{-\beta H_0} \right] = e^{-\beta H_0} \int_0^\beta d\lambda e^{\lambda H_0} \left[H_0, \hat{A} \right] e^{-\lambda H_0} \quad (\text{A6})$$

$$= -i\hbar e^{-\beta H_0} \int_0^\beta d\lambda \dot{\hat{A}}(-i\hbar\lambda), \quad (\text{A7})$$

where $\hat{A}(t) = e^{-H_0 t/i\hbar} \hat{A}(0) e^{H_0 t/i\hbar}$ is the time-dependent operator, and the Heisenberg equation is used for the second line. The retarded Green's function can be written as

$$G^R(\hat{A}(t), \hat{B}) = \frac{1}{i\hbar} \left\langle \left[\hat{A}(t), \hat{B}(0) \right] \right\rangle \quad (\text{A8})$$

$$= \frac{1}{i\hbar} \text{Tr} \rho \left[\hat{A}(t), \hat{B}(0) \right] \quad (\text{A9})$$

$$= \frac{1}{i\hbar} \text{Tr} \left[\rho, \hat{A}(t) \right] \hat{B}(0) \quad (\text{A10})$$

where $\rho = e^{-\beta H_0}/Z$ is the density matrix, and we used the cyclicity of the trace in the second line. Substituting Eq. (A7) into Eq. (A10), we obtain the relation between the retarded Green's function and the canonical correlation function as

$$G^R(\hat{A}(t), \hat{B}) = \text{Tr} \rho \int_0^\beta d\lambda \hat{B}(-i\hbar\lambda) \dot{\hat{A}}(t) \quad (\text{A11})$$

$$= \beta \left\langle \hat{B}; \dot{\hat{A}}(t) \right\rangle_{\text{can}} \quad (\text{A12})$$

$$= \beta \frac{d}{dt} \left\langle \hat{B}; \hat{A}(t) \right\rangle_{\text{can}}. \quad (\text{A13})$$

In the harmonic approximation, we replace the canonical correlation function with the classical correlation function

$$C(t) = \langle A(t)B(0) \rangle. \quad (\text{A14})$$

As a result, the dielectric function becomes

$$\varepsilon_{\alpha\beta}(\omega) = \varepsilon_{\alpha\beta}^\infty - \frac{\beta}{V} \int_0^\infty \frac{d \langle M_\alpha(t) M_\beta(0) \rangle}{dt} e^{-i\omega t} dt. \quad (\text{A15})$$

The ensemble average can be calculated from the time average of the MD calculations with the assumption of ergodicity. The mean value of dipole moments is assumed to be zero. If the dipole has a nonzero mean value, we simply subtract the mean value from the total dipole as

$$\bar{\mathbf{M}} = \mathbf{M} - \langle \mathbf{M} \rangle. \quad (\text{A16})$$

The dielectric function of an isotropic and homogeneous fluid can be calculated by averaging diagonal components of Eq. (A15) as

$$\varepsilon(\omega) = \frac{\varepsilon_{11}(\omega) + \varepsilon_{22}(\omega) + \varepsilon_{33}(\omega)}{3} \quad (\text{A17})$$

$$= \varepsilon^\infty - \frac{1}{3k_B T V} \int_0^\infty \frac{d \langle \mathbf{M}(t) \cdot \mathbf{M}(0) \rangle}{dt} e^{-i\omega t} dt. \quad (\text{A18})$$

[1] K. Shinokita, A. V. Cunha, T. L. C. Jansen, and M. S. Pshenichnikov, *The Journal of Chemical Physics* **142**, 212450 (2015).

[2] M. Jorge, J. R. B. Gomes, and M. C. Barrera, *Journal of Molecular Liquids* **356**, 119033 (2022).

[3] D. W. Davidson, *Canadian Journal of Chemistry* **35**, 458 (1957).

- [4] S. Carlson, F. N. Brünig, P. Loche, D. J. Bonthuis, and R. R. Netz, *The Journal of Physical Chemistry A* **124**, 5599 (2020).
- [5] B. Guillot, P. Marteau, and J. Obriot, *The Journal of Chemical Physics* **93**, 6148 (1990).
- [6] J. E. Bertie, S. L. Zhang, H. H. Eysel, S. Baluja, and M. K. Ahmed, *Applied Spectroscopy* **47**, 1100 (1993).
- [7] J. E. Bertie and S. L. Zhang, *The Journal of Chemical Physics* **101**, 8364 (1994).
- [8] J. E. Bertie and S. L. Zhang, *Journal of Molecular Structure Structural Chemistry*, **413–414**, 333 (1997).
- [9] T. Fukasawa, T. Sato, J. Watanabe, Y. Hama, W. Kunz, and R. Buchner, *Physical Review Letters* **95**, 197802 (2005).
- [10] S. Sarkar, D. Saha, S. Banerjee, A. Mukherjee, and P. Mandal, *Chemical Physics Letters* **678**, 65 (2017).
- [11] Y. Yomogida, Y. Sato, R. Nozaki, T. Mishina, and J. Nakahara, *Journal of Molecular Liquids* **154**, 31 (2010).
- [12] Y. Yomogida, Y. Sato, R. Nozaki, T. Mishina, and J. Nakahara, *Journal of Molecular Structure* **981**, 173 (2010).
- [13] H. Shirota, K. Yoshihara, N. A. Smith, S. Lin, and S. R. Meech, *Chemical Physics Letters* **281**, 27 (1997).
- [14] A. Rahman, *Physical Review* **136**, A405 (1964).
- [15] R. Kubo, *Journal of the Physical Society of Japan* **12**, 570 (1957).
- [16] M. Matsumoto and K. E. Gubbins, *The Journal of Chemical Physics* **93**, 1981 (1990).
- [17] M. S. Skaf, T. Fonseca, and B. M. Ladanyi, *The Journal of Chemical Physics* **98**, 8929 (1993).
- [18] B. M. Ladanyi and M. S. Skaf, *The Journal of Physical Chemistry* **100**, 1368 (1996).
- [19] D. S. Venables and C. A. Schmuttenmaer, *The Journal of Chemical Physics* **113**, 3249 (2000).
- [20] G. Pálinkás, I. Bakó, K. Heinzinger, and P. Bopp, *Molecular Physics* **73**, 897 (1991).
- [21] G. Garberoglio, R. Vallauri, and G. Sutmann, *The Journal of Chemical Physics* **117**, 3278 (2002).
- [22] G. Garberoglio and R. Vallauri, *The Journal of Chemical Physics* **115**, 395 (2001).
- [23] J. Martí, J. A. Padró, and E. Guàrdia, *Journal of Molecular Liquids Ultrafast Phenomena in Liquids and Glasses*, **64**, 1 (1995).
- [24] H. Torii, *Journal of Molecular Liquids* **390**, 123111 (2023).
- [25] I. Y. Shilov, *Molecular Physics* **113**, 570 (2015).
- [26] T. Kulschewski and J. Pleiss, *Molecular Simulation* **39**, 754 (2013).
- [27] R. Car and M. Parrinello, *Physical Review Letters* **55**, 2471 (1985).
- [28] R. Resta, *Ferroelectrics* **136**, 51 (1992).
- [29] R. D. King-Smith and D. Vanderbilt, *Physical Review B* **47**, 1651 (1993).
- [30] N. Marzari and D. Vanderbilt, *Physical Review B* **56**, 12847 (1997).
- [31] N. Marzari, A. A. Mostofi, J. R. Yates, I. Souza, and D. Vanderbilt, *Reviews of Modern Physics* **84**, 1419 (2012).
- [32] E. Tsuchida, Y. Kanada, and M. Tsukada, *Chemical Physics Letters* **311**, 236 (1999).
- [33] E. Tsuchida, *Journal of Physics: Condensed Matter* **20**, 294212 (2008).
- [34] J.-W. Handgraaf, T. S. van Erp, and E. J. Meijer, *Chemical Physics Letters* **367**, 617 (2003).
- [35] M. J. McGrath, I.-F. W. Kuo, and J. I. Siepmann, *Physical Chemistry Chemical Physics* **13**, 19943 (2011).
- [36] M. J. McGrath, I.-F. W. Kuo, J. N. Ghogomu, C. J. Mundy, and J. I. Siepmann, *The Journal of Physical Chemistry B* **115**, 11688 (2011).
- [37] M. Pagliai, G. Cardini, R. Righini, and V. Schettino, *The Journal of Chemical Physics* **119**, 6655 (2003).
- [38] V. K. Yadav, A. Karmakar, J. R. Choudhuri, and A. Chandra, *Chemical Physics* **408**, 36 (2012).
- [39] A. Jindal and S. Vasudevan, *Physical Chemistry Chemical Physics* **22**, 6690 (2020).
- [40] D. Hait and M. Head-Gordon, *Journal of Chemical Theory and Computation* **14**, 1969 (2018).
- [41] J.-W. Handgraaf, E. J. Meijer, and M.-P. Gaijeot, *The Journal of Chemical Physics* **121**, 10111 (2004).
- [42] K. N. Woods and H. Wiedemann, *The Journal of Chemical Physics* **123**, 134506 (2005).
- [43] N. Sieffert, M. Bühl, M.-P. Gaijeot, and C. A. Morrison, *Journal of Chemical Theory and Computation* **9**, 106 (2013).
- [44] C. C. Wang, J. Y. Tan, and L. H. Liu, *AIP Advances* **7**, 035115 (2017).
- [45] Michael. Haughney, Mauro. Ferrario, and I. R. McDonald, *The Journal of Physical Chemistry* **91**, 4934 (1987).
- [46] M. Sharma, R. Resta, and R. Car, *Physical Review Letters* **95**, 187401 (2005).
- [47] W. Chen, M. Sharma, R. Resta, G. Galli, and R. Car, *Physical Review B* **77**, 245114 (2008).
- [48] J. Behler and M. Parrinello, *Physical Review Letters* **98**, 146401 (2007).
- [49] J. Behler, *International Journal of Quantum Chemistry* **115**, 1032 (2015).
- [50] H. Wang, L. Zhang, J. Han, and W. E, *Computer Physics Communications* **228**, 178 (2018).
- [51] J. Zeng, D. Zhang, D. Lu, P. Mo, Z. Li, Y. Chen, M. Rynik, L. Huang, Z. Li, S. Shi, Y. Wang, H. Ye, P. Tuo, J. Yang, Y. Ding, Y. Li, D. Tisi, Q. Zeng, H. Bao, Y. Xia, J. Huang, K. Muraoka, Y. Wang, J. Chang, F. Yuan, S. L. Bore, C. Cai, Y. Lin, B. Wang, J. Xu, J.-X. Zhu, C. Luo, Y. Zhang, R. E. A. Goodall, W. Liang, A. K. Singh, S. Yao, J. Zhang, R. Wentzcovitch, J. Han, J. Liu, W. Jia, D. M. York, W. E, R. Car, L. Zhang, and H. Wang, *The Journal of Chemical Physics* **159**, 054801 (2023).
- [52] N. Artrith and A. Urban, *Computational Materials Science* **114**, 135 (2016).
- [53] M. Gastegger, J. Behler, and P. Marquetand, *Chemical Science* **8**, 6924 (2017).
- [54] R. Beckmann, F. Briec, C. Schran, and D. Marx, *Journal of Chemical Theory and Computation* **18**, 5492 (2022).
- [55] T. Bereau, R. A. DiStasio, Jr., A. Tkatchenko, and O. A. von Lilienfeld, *The Journal of Chemical Physics* **148**, 241706 (2018).
- [56] D. P. Metcalf, A. Jiang, S. A. Spronk, D. L. Cheney, and C. D. Sherrill, *Journal of Chemical Information and Modeling* **61**, 115 (2021).
- [57] P. Bleiziffer, K. Schaller, and S. Riniker, *Journal of Chemical Information and Modeling* **58**, 579 (2018).
- [58] K. Yao, J. E. Herr, D. W. Toth, R. Mckintyre, and J. Parkhill, *Chemical Science* **9**, 2261 (2018).

- [59] O. T. Unke and M. Meuwly, *Journal of Chemical Theory and Computation* **15**, 3678 (2019).
- [60] V. Kapil, D. M. Wilkins, J. Lan, and M. Ceriotti, *The Journal of Chemical Physics* **152**, 124104 (2020).
- [61] M. Veit, D. M. Wilkins, Y. Yang, R. A. DiStasio, and M. Ceriotti, *The Journal of Chemical Physics* **153**, 024113 (2020).
- [62] R. Hou, Y. Quan, and D. Pan, *The Journal of Chemical Physics* **153**, 101103 (2020).
- [63] Z. L. Glick, A. Koutsoukas, D. L. Cheney, and C. D. Sherrill, *The Journal of Chemical Physics* **154**, 224103 (2021).
- [64] M. Thürlmann, L. Bösel, and S. Riniker, *Journal of Chemical Theory and Computation* **18**, 1701 (2022).
- [65] Y. Zhong, H. Yu, X. Gong, and H. Xiang, *The Journal of Physical Chemistry Letters*, 6339 (2023).
- [66] A. Krishnamoorthy, K.-i. Nomura, N. Baradwaj, K. Shimamura, P. Rajak, A. Mishra, S. Fukushima, F. Shimojo, R. Kalia, A. Nakano, and P. Vashishta, *Physical Review Letters* **126**, 216403 (2021).
- [67] L. Zhang, M. Chen, X. Wu, H. Wang, W. E, and R. Car, *Physical Review B* **102**, 041121 (2020).
- [68] G. M. Sommers, M. F. C. Andrade, L. Zhang, H. Wang, and R. Car, *Physical Chemistry Chemical Physics* **22**, 10592 (2020).
- [69] L. Zhang, H. Wang, M. C. Muniz, A. Z. Panagiotopoulos, R. Car, and W. E, *The Journal of Chemical Physics* **156**, 124107 (2022).
- [70] M. Neumann and O. Steinhauser, *Chemical Physics Letters* **102**, 508 (1983).
- [71] M. Neumann, O. Steinhauser, and G. S. Pawley, *Molecular Physics* [10.1080/00268978400101081](https://doi.org/10.1080/00268978400101081) (1984).
- [72] M. Neumann and O. Steinhauser, *Chemical Physics Letters* **106**, 563 (1984).
- [73] M. Sharma, R. Resta, and R. Car, *Physical Review Letters* **98**, 247401 (2007).
- [74] J. Cardona, M. B. Sweatman, and L. Lue, *The Journal of Physical Chemistry B* **122**, 1505 (2018).
- [75] E. Hecht, *Optics* (Pearson Education, Incorporated, 2017).
- [76] U. E. N. C. f. E. Assessment, *CRC Handbook of Chemistry and Physics* (2009).
- [77] A. P. Gregory and R. N. Clarke, *Tables of the Complex Permittivity of Dielectric Reference Liquids at Frequencies up to 5 GHz.* (Teddington, 2001).
- [78] J. L. Hales and J. H. Ellender, *The Journal of Chemical Thermodynamics* **8**, 1177 (1976).
- [79] Car-Parrinello Molecular Dynamics.
- [80] C. Lee, W. Yang, and R. G. Parr, *Physical Review B* **37**, 785 (1988).
- [81] A. D. Becke, *Physical Review A* **38**, 3098 (1988).
- [82] S. Grimme, *Journal of Computational Chemistry* **27**, 1787 (2006).
- [83] S. Goedecker, M. Teter, and J. Hutter, *Physical Review B* **54**, 1703 (1996).
- [84] M. J. Abraham, T. Murtola, R. Schulz, S. Páll, J. C. Smith, B. Hess, and E. Lindahl, *SoftwareX* **1–2**, 19 (2015).
- [85] J. Wang, R. M. Wolf, J. W. Caldwell, P. A. Kollman, and D. A. Case, *Journal of Computational Chemistry* **25**, 1157 (2004).
- [86] A. Jakalian, D. B. Jack, and C. I. Bayly, *Journal of Computational Chemistry* **23**, 1623 (2002).
- [87] J. Wang, W. Wang, P. A. Kollman, and D. A. Case, *Journal of Molecular Graphics and Modelling* **25**, 247 (2006).
- [88] A. W. Sousa da Silva and W. F. Vranken, *BMC Research Notes* **5**, 367 (2012).
- [89] L. Martínez, R. Andrade, E. G. Birgin, and J. M. Martínez, *Journal of Computational Chemistry* **30**, 2157 (2009).
- [90] A. Paszke, S. Gross, F. Massa, A. Lerer, J. Bradbury, G. Chanan, T. Killeen, Z. Lin, N. Gimelshein, L. Antiga, A. Desmaison, A. Köpf, E. Yang, Z. DeVito, M. Raison, A. Tejani, S. Chilamkurthy, B. Steiner, L. Fang, J. Bai, and S. Chintala, *PyTorch: An Imperative Style, High-Performance Deep Learning Library* (2019), [arXiv:1912.01703](https://arxiv.org/abs/1912.01703) [cs, stat].
- [91] A. F. Agarap, *Deep Learning using Rectified Linear Units (ReLU)* (2019), [arXiv:1803.08375](https://arxiv.org/abs/1803.08375) [cs, stat].
- [92] D. P. Kingma and J. Ba, *Adam: A Method for Stochastic Optimization* (2017), [arXiv:1412.6980](https://arxiv.org/abs/1412.6980) [cs].
- [93] <https://github.com/ToAmamo/MLWC>.
- [94] E. U. Franck and R. Deul, *Faraday Discussions of the Chemical Society* **66**, 191 (1978).
- [95] E. Sani and A. Dell’Oro, *Optical Materials* **60**, 137 (2016).
- [96] P. L. Silvestrelli and M. Parrinello, *Physical Review Letters* **82**, 3308 (1999).
- [97] E. B. Freyer, J. C. Hubbard, and D. H. Andrews, *Journal of the American Chemical Society* **51**, 759 (1929).
- [98] I. Doroshenko, V. Pogorelov, and V. Sablinskas, *Dataset Papers in Science* **2013**, e329406 (2012).
- [99] E. K. Plyler, *Journal of Research of the National Bureau of Standards* **48**, 281 (1952).
- [100] R. Ramírez, T. López-Ciudad, P. Kumar P, and D. Marx, *The Journal of Chemical Physics* **121**, 3973 (2004).
- [101] R. Iftimie and M. E. Tuckerman, *The Journal of Chemical Physics* **122**, 214508 (2005).